Original Article

Optical coherence tomography angiography monitors human cutaneous wound healing over time

Anthony J. Deegan[1], Wendy Wang[1], Shaojie Men[1], Yuandong Li[1], Shaozhen Song[1], Jingjiang Xu[1], Ruikang K. Wang[1,2]

[1]Department of Bioengineering, [2]Department of Ophthalmology, University of Washington, Seattle, Washington, USA

Correspondence to: Ruikang K. Wang. Department of Bioengineering, University of Washington, 3720 15th Ave. NE, Seattle, Washington 98195, USA. Email: wangrk@uw.edu.

Background: *In vivo* imaging of the complex cascade of events known to be pivotal elements in the healing of cutaneous wounds is a difficult but essential task. Current techniques are highly invasive, or lack the level of vascular and structural detail required for accurate evaluation, monitoring and treatment. We aimed to use an advanced optical coherence tomography (OCT)-based angiography (OCTA) technique for the non-invasive, high resolution imaging of cutaneous wound healing.

Methods: We used a clinical prototype OCTA to image, identify and track key vascular and structural adaptations known to occur throughout the healing process. Specific vascular parameters, such as diameter and density, were measured to aid our interpretations under a spatiotemporal framework.

Results: We identified multiple distinct, yet overlapping stages, hemostasis, inflammation, proliferation, and remodeling, and demonstrated the detailed vascularization and anatomical attributes underlying the multifactorial processes of dermatologic wound healing.

Conclusions: OCTA provides an opportunity to both qualitatively and quantitatively assess the vascular response to acute cutaneous damage and in the future, may help to ascertain wound severity and possible healing outcomes; thus, enabling more effective treatment options.

Keywords: Optical coherence tomography angiography (OCTA); skin; wound healing; microvasculature

Submitted Feb 08, 2018. Accepted for publication Feb 08, 2018.
doi: 10.21037/qims.2018.02.07
View this article at: http://dx.doi.org/10.21037/qims.2018.02.07

Introduction

The accurate assessment of cutaneous wounds, such as burns, chronic skin ulcers, and surgical wounds, is critical if an effective treatment plan is to be prescribed. If misdiagnosed, hindered or ineffective, wound healing may increase the risk of scarring and/or infection, which can lead to morbidity or even death (1). The process of wound healing involves a highly coordinated cascade of events comprising multiple cell types, bioactive molecules, and extracellular matrix proteins (2) to form four distinct, yet overlapping phases: hemostasis, inflammation, proliferation, and remodeling (3). The skin's microvasculature plays a pivotal role in each of the various stages of wound healing, as it regulates blood flow and tissue perfusion, facilitates oxygen and nutrient delivery, and supports granulation tissue formation (4). Therefore, identifying and accurately assessing the characteristic vascular changes that occur throughout each phase and correlating them with structural changes could provide a basis for wound healing assessment. For example, monitoring the vascular features associated with re-epithelialization, reformation of the dermal-epidermal junction, the subsequent thickening of the newly formed epidermis, and dermal remodeling could be used to as indicators for normal wound healing (5). Additionally, any deviations from normal could be addressed with treatment adjustments to ensure optimal recovery.

Typically, visual observations and surface measurements

have been used to evaluate wound healing via the monitoring of wound size, color, odor, drainage and eschar (6,7). Such measurements, however, are restricted to the skin's surface and depend heavily on the experience of medical professionals, wound condition and treatment history (8). Attempts have been made to quantify such measurements, such as with the use of the Vancouver scar scale and the Manchester scar proforma, but these too suffer from significant subjective drawbacks (9,10). Currently, biopsies provide the best objective assessment of wound recovery, but this technique causes further tissue destruction and increases the risk of infection (11). With that, various techniques and technologies have been explored for the quantitative evaluation of wound healing, particularly burn wound healing, such as the use of magnetic resonance imaging (MRI) (12), ultrasound imaging (13), fluorescence imaging (14), polarization-sensitive optical coherence tomography (PS-OCT) (15,16), and laser Doppler flowmetry (LDF) and perfusion imaging (17,18). To date, however, no technique is without its disadvantages, and whilst LDF is proving the most popular non-invasive imaging technique, its limited sensitivity concerning various wound conditions and lack of three-dimensional (3D) imaging capabilities have restricted its use clinically (19).

The continued development of OCT technology over recent years has significantly increased its use in a variety of fields, both research and clinically driven. Although a well-established diagnostic tool in the field of ophthalmology (20,21), modern technical advances, such as an increased resolution via improved laser sources (22), enhanced sensitivity through the use of phase information (23-25), accelerated scanning speeds (26,27) and a larger field-of-view (28,29), have enabled the exploration of OCT applications in dermatology (30,31). With regards to cutaneous repair or regeneration, for example, OCT has been used in conjunction with other techniques, such as multiphoton microscopy and histopathology, to monitor over time wound healing in mice (5), wound healing in an engineered skin equivalent tissue model (32), and scar formation during skin substitute-assisted wound healing (33). It has proven itself particularly useful in determining cutaneous burn severity (19,34) because whilst the light signal is attenuated as it propagates through the skin due to multiple scattering by protein components, thermally damaged collagen changes the magnitude of light attenuation (32); thus, allowing for the establishment of burn severity via the measurement of burn depth (15). The determining of burn depth is especially relevant for treatment planning and is a major factor in long term prognosis (35,36). Unlike first and third degree burns where treatment options are typically predetermined, i.e., unaided spontaneous healing *vs.* skin grafting, respectively, second degree burns are often more complicated to treat because surgeons have to wait to evaluate if the wound can heal unaided before a decision is made regarding surgical intervention, i.e., skin grafting, meaning the chances of infection are heightened (34). The use of OCT can aid in the earliest evaluations of burn severity, negating the need to wait for signs of healing; thus, accelerating treatment and subsequent recovery.

Furthermore, a more profound examination of the OCT signal can provide additional information beyond the visualization of tissue structure (37). Since signals derived from tissue regions with moving particles, such as blood vessels, contain larger variance compared to those from static tissue, one could contrast said regions within complex OCT signals. This allows for the identification of functional blood vessels within tissue by isolating the scattering properties of moving red blood cells (21,38,39). The use of OCT in such a way constitutes a suite of OCT-based angiography (OCTA) technologies (21,40). There are a number of approaches one could use to contrast vasculature, each with its own advantages, but of interest here is a complex-signal based method because it provides more sensitive measurement to slow blood flow, such as in the functional capillary vessels (41,42). One such method whose high sensitivity has already been shown to be successful in the visualization of functional vasculatures in small animal models and human tissues, such as skin and eye (43-45) is optical microangiography (OMAG) (39,46-48). The recent development of OMAG for imaging dynamic blood perfusion within tissue beds was heralded as one of the most significant extensions of conventional OCT, and has been successfully translated to clinical ophthalmic imaging (45,49-51). Here, we present a clinical prototype OMAG system that was specially designed for dermatological applications for high resolution monitoring of the microcirculatory and structural features underlying the processes of wound healing in otherwise healthy skin.

Methods

Subject volunteer

The injury was sustained when a piece of molten plastic accidentally fell onto the skin of the subject's right hand.

Upon realizing the injury, the subject attempted to remove the offending plastic, with which, the epidermal layer of skin was removed. Scanning commenced ~48 hours after the incident took place. Informed written consent was obtained from the subject volunteer prior to imaging and the use of OCT laboratory equipment was approved by the Institutional Review Board of the University of Washington.

OCTA prototype system

For this study, we used an in-house-built, clinical prototype swept source-OCT (SS-OCT) system, as shown in *Figure 1A*. The system setup was similar to that used in a previous study in our lab (52). In short, a 200-kHz vertical-cavity surface-emitting (VCSEL) swept laser source (SL1310V1-20048, Thorlabs Inc., Newton, USA) was used as the light source providing a central wavelength of 1,310 nm (infrared/IR) and a spectral bandwidth of 100 nm, giving an axial resolution of ~8 μm in tissue (~11 μm in air). The sample arm consisted of a hand-held probe, where a paired X-Y galvo scanner and sample optics assembly were housed. To facilitate scanning, a monitoring screen was integrated with the hand-held where the OCT and OCTA cross-sectional images are displayed in real time to aid the operator during imaging. In this study, the probe was affixed with a sample spacer to maintain a consistent distance between the objective lens and the skin. A disposable glass cover plate was attached to the spacer to support even, comfortable contact with the skin. A 5X objective lens within the hand-held probe focused the IR light source into a beam spot on the skin with an incident power of 5 mW, similar to that of a common laser pointer. Alongside the IR light source was a visible laser beam, which was used to guide OCTA imaging, which also provided an opportunity to position and orientate the beam spot over the same area of skin for each scan session, producing reliable and repeatable scans over different time points (53). The field-of-view was 10×10 mm^2 with a penetration depth of ~1.5 mm.

Imaging protocol

The specific area of skin intended for scanning was located on the dorsum of the right hand, over the first dorsal interosseous between the thumb and index finger. For scanning, the hand-held probe was positioned approximately perpendicular to the wound. Prior to scanning, a drop of glycerin was placed on the skin to act as a refractive index matching medium (54). Scanning was carried out at 2, 5, 9, 16, 23 and 44 days post-injury. Each scanning session, including preparation, required 30–40 minutes, approximately, as multiple scans were taken of the wound during each session for quantitative purposes with each 3D scan taking ~6 seconds. Multiple scans were also taken of the healthy skin adjacent to the wound for comparative purposes.

High resolution 3D OCT (*Figure 1B*) and OCTA (*Figure 1C*) images were generated for tissue structure and vascular visualization, respectively, with the following scanning protocol. Firstly, reflectivity profiles of skin depth, i.e., A-lines, were acquired consecutively (10 μm apart) along the fast scanning axis to produce a two-dimensional (2D) cross-sectional image, i.e., B-frame. Each B-frame scan was repeated four times at the same position for vascular information extraction using OMAG algorithm (46). Numerical phase-stabilization algorithms were also applied to the complex data for enhanced angiography contrast (52). Next, consecutive cross-sectional positions (10 μm apart) were scanned along a perpendicular axis to the fast axis, i.e., slow axis, to yield a 3D volume scan, i.e., C-scan. A final volumetric dataset comprised 1,000 A-lines and 1,000 cross-sectional positions (4,000 B-frames), covering a region of 10×10 mm^2 of skin. From the volumetric scans, 3D tissue structure was constructed, as shown in *Figure 1B*. In addition, for improved 3D vascular mapping, each 3D volume scan was repeated four times to enhance visualization of actively alternating capillary perfusion. The four volumes were then combined via 3D registration, followed by averaging, to produce a single, high resolution 3D OCT/OCTA volume scan, using a proprietary algorithm developed in our lab. Each OCT/OCTA volume scan is presented here as an X-Y maximum intensity projection (MIP) *en face* projected image. Where applicable, a color code was applied to *en face* projected vasculature to denote vessel depth.

Image segmentation

To gain a better insight into how vascular and structural features might differ at various depths during healing, the OCTA volume scans were segmented to reveal separated slabs of skin. To do this, we employed a semi-automatic segmentation software that was previously used and validated in ophthalmology to segment retinal layers (55), and modified it for the purposes of segmenting skin layers. Based on OCT structural features of epidermis and dermis layers, the software segmented each of the OCTA volume

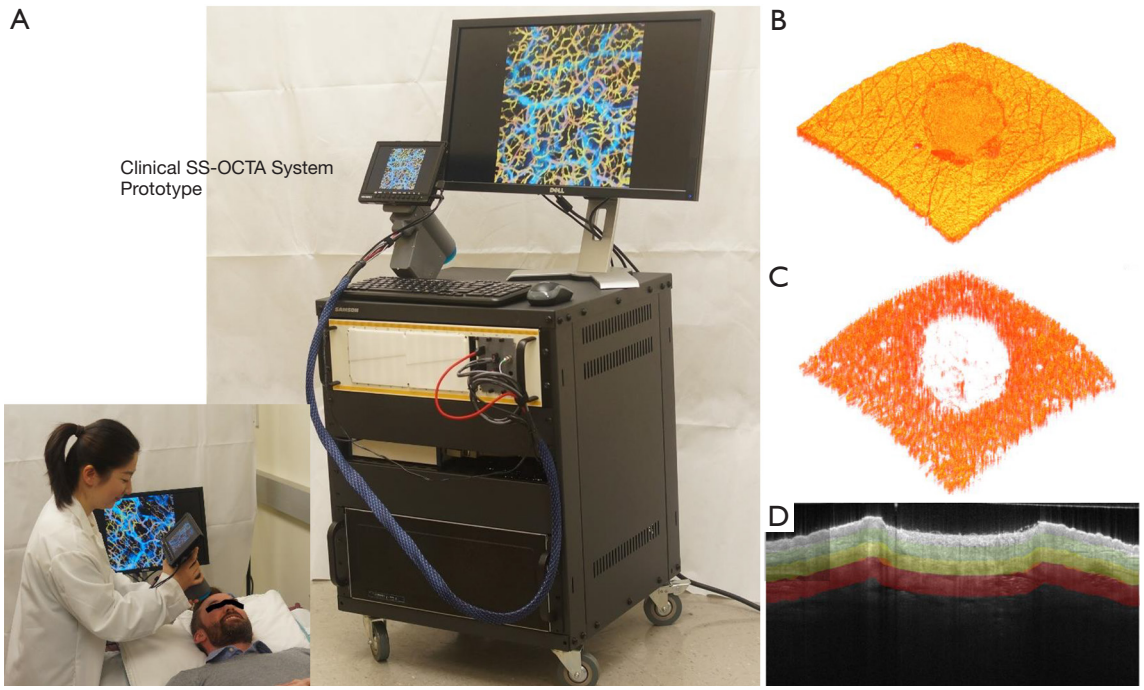

Figure 1 Clinical prototype OCTA system alongside the imaging and data collection protocols. (A) Photograph showing the clinical prototype swept-source OCTA system; (B) a 3D OCTA volume scan showing a wound in the skin; (C) the vascular data derived from the 3D OCTA volume scan depicted in (B); (D) a cross-sectional B-frame selected from (B) highlighting three layers where segmentation is carried out. OCTA, optical coherence tomography-based angiography.

scans into three slabs with depths of 265–530, 530–795, and 795–1,200 μm, thought to represent the papillary dermis, lower papillary/upper reticular dermis, and reticular dermis layers, respectively. Illustrated in *Figure 1D* is an example of such slabs highlighted by colored regions in one structural B-frame. Both the vascular and structural volumes were segmented at these depths based on structural features before being *en face* projected for convenient monitoring.

Quantification of the vascular response

To quantify the vascular response, vascular parameters, such as vessel diameter and functional vessel density changes over time, were measured. This was carried out using a quantification algorithm previously developed by Reif *et al.* (56) and further explained by Chu *et al.* (57). Quantification was carried out on all three vascular slabs obtained from segmentation. These analyses were carried out in two ways. First, vessel diameter was quantified for the whole scan area, i.e., taking both the wound and surrounding skin into account, over time. Given the significant role played by peripheral vasculature during healing, this method allowed for a comprehensive overview of the whole healing process. Second, positive and negative masks of the wound were created for more region-specific vascular measurements to be taken (*Figure 2*). This allowed for healing to be measured directly within the wound and indirectly in the surrounding skin. The masks were created using the *en face* projected OCT structural image of the wound at its earliest time point as a template. Simply, the outline of the wound was traced to produce positive and negative masks (*Figure 2A*,*B*). The masks were checked to ensure they accurately represented the wound on all three vascular layers. The control scans were masked also to ensure continuity. *Figure 2C*,*D* show the negative mask and its application to the papillary dermis layer of a control scan. This allowed for vessel diameter and functional vessel density changes to be measured solely within the wound itself, and/or within an equivalent control site. *Figure 2E*,*F* show the positive mask and its application to the same control scan shown in *Figure 2D*. This allowed for vessel diameter and functional vessel density changes to be measured solely within the surrounding skin of the wound, and/or within an equivalent control site.

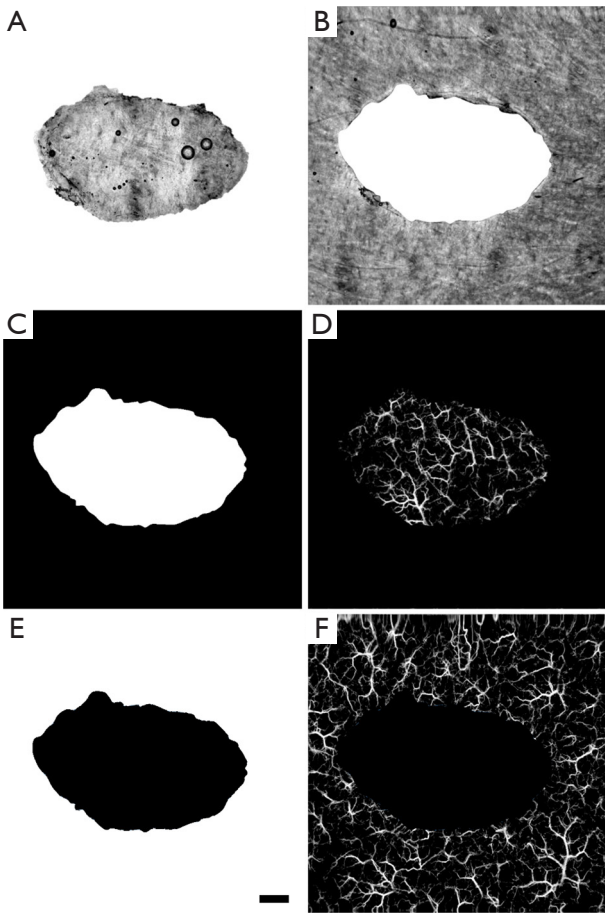

Figure 2 Mask preparation for quantification of vessel parameters inside and outside the wound. (A) A positive mask derived from a MIP *en face* projected structural image of the wound; (B) a negative mask correlating to the positive mask depicted in (A); (C) the final negative mask prior to application to a MIP *en face* projected vascular image for quantification. This allowed for quantification of vessel parameters solely within the wound; (D) a MIP *en face* projected vascular image of a control scan with the negative mask depicted in (C) applied; (E) the final positive mask prior to application to a MIP *en face* projected vascular image for quantification. This allowed for quantification of vessel parameters solely outside of the wound; (F) a MIP *en face* projected vascular image of a control scan with the positive mask depicted in (E) applied. Scale bar represents 1 mm. MIP, maximum intensity projection.

Statistical analysis

A minimum of three *en face* images, each derived from a separate 3D-registered 3D OCT volume scans, per variable were used for statistical analysis. Data was averaged and represented as a mean value ± standard error of the mean (SEM). Groups were compared using *t*-tests and one-way analysis of variance (ANOVA). A P value below 0.05 was denoted to indicate statistical significance. In graphs, statistical significance is indicated at four levels: *, P≤0.05; **, P≤0.01; ***, P≤0.001; and ****, P≤0.0001.

Results

The data presented here outlines alterations from normal to vascular and structural features of the skin using a spatiotemporal framework.

Temporal vascular features

Figure 3 shows the overall summary of the results over 44 days of the same wound alongside the adjacent control site, displayed in *en face* OCTA (*Figure 3A*,*B*,*C*,*D*,*E*), and corresponding *en face* OCT structural images (*Figure 3F*,*G*,*H*,*I*,*J*), and selected B-frame OCTA and OCT images (*Figure 3K*,*L*,*M*,*N*,*O*). Also displayed are the results captured from normal skin (left column) for comparison.

The *en face* projection of the vasculature of normal skin (*Figure 3A*) typically gives homogenous vascular distribution. Shown in *Figure 3K* is the cross-sectional B-frame of the vasculature of normal skin (top), together with corresponding structure (bottom), obtained at the perforated red line in (A), which again shows a relatively homogenous vessel distribution, besides vessel diameter expectedly increasing with depth (58).

Shown in *Figure 3B*,*C*,*D*,*E* are the selected *en face* projected vascular maps of the skin during healing at time points post-injury as shown. Compared to normal skin, dilated vessels surrounding and immediately below the wound can be seen in *Figure 3B*,*C*. In *Figure 3C*,*D*, angiogenic vessels can be seen migrating into the wound, with the latter image, *Figure 3D*, showing more developed vascular sprouts. A reduction in peripheral vasodilation can also be seen in *Figure 3D* with deeper, large vessels now appearing within the wound. In *Figure 3E*, angiogenic vessels are no longer visible and vasodilation appears only in the wound area. Shown in the top of *Figure 3K*,*L*,*M*,*N*,*O* are the cross-sectional B-frames corresponding to the perforated red lines in *en face* images, respectively. Each of the vascular features previously mentioned are corroborated here with one interesting addition. Shown in *Figure 3L*,*M* are two bright regions visible immediately below the wound. This is thought to represent the presence of thermally damaged collagen. This feature is lost in *Figure 3N*,*O*.

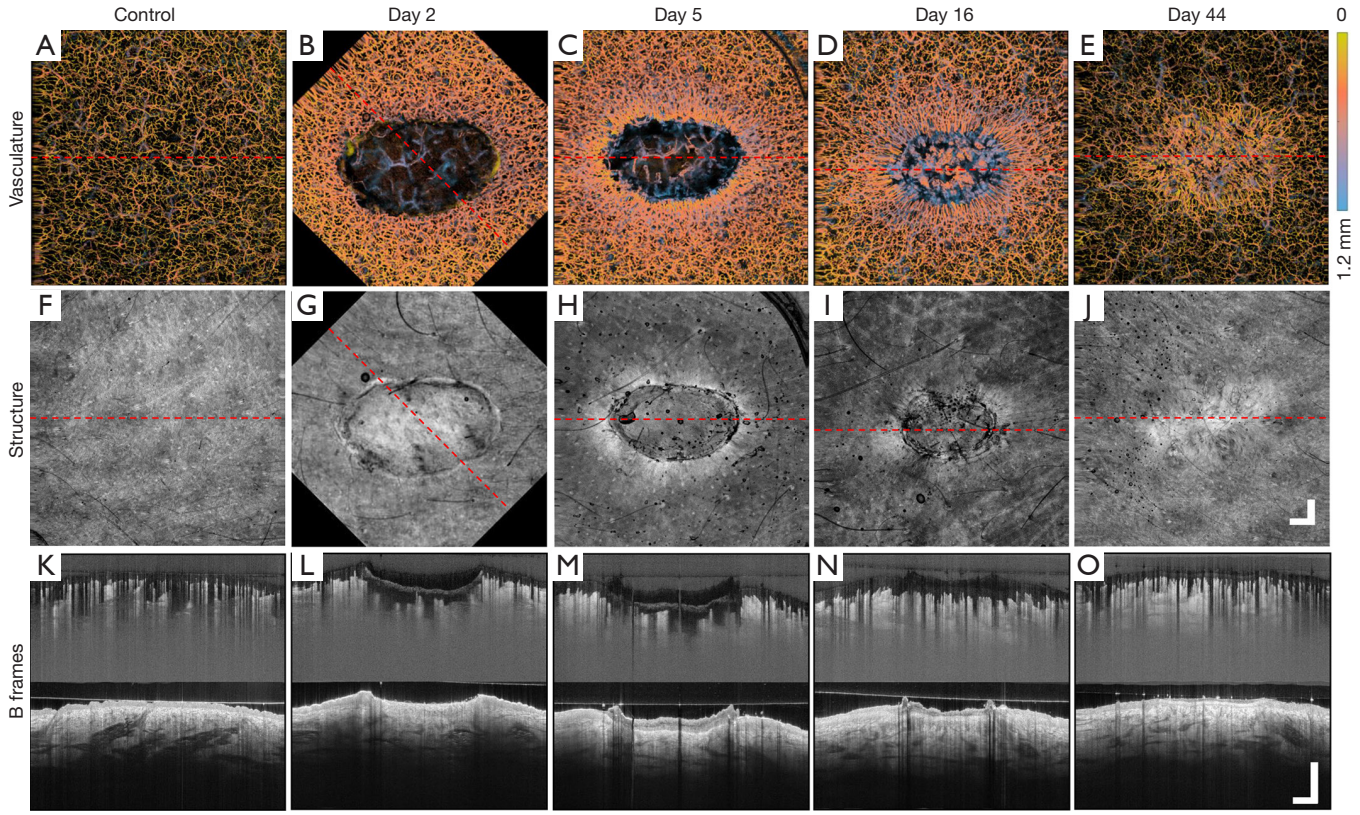

Figure 3 MIP *en face* projected whole volume scans presenting the vascular and structural features of normal and healing skin. (A,B,C,D,E) MIP *en face* projected vascular images during normal and healing states. Color bar on the right side represents vessel depth; (F,G,H,I,J) MIP *en face* projected structural images during normal and healing states. The red dotted line on each *en face* image indicates where the corresponding cross-sectional B-frames were taken from; (K,L,M,N,O) cross-sectional B-frames of the vasculature (top part) and structure (bottom part) during normal and healing states, respectively. Shown is the vasculature and structure of acutely wounded skin healing/returning to a state similar to that of normal skin. Scale bar represents 1 mm. MIP, maximum intensity projection.

Temporal structural features

The *en face* projection of the structure of normal skin (*Figure 3F*) shows the topographically smooth structure of the skin. Shown in *Figure 3K* (bottom) is the cross-sectional B-frame of the structure of normal skin corresponding to the perforated red line in *Figure 3F*, which shows an intact epidermis with a consistent thickness and homogenous structural brightness, besides an increased brightness immediately below the epidermis thought to represent the highly organized extracellular matrix of the papillary dermis (59).

Shown in *Figure 3G,H,I,J* are the *en face* projected structures of the skin during healing. A fibrin clot can clearly be seen in *Figure 3G*, which later becomes an eschar in *Figure 3H*. The tissue immediately surrounding the wound appears brighter (*Figure 3G*) and progressive wound contraction can be seen in *Figure 3H,I,J*, respectively. The wound itself is no longer visible in *Figure 3J*, aside from swirled patterns, most likely due to increased collagen production as collagen type III was being turned over to type I. Shown in the bottom of *Figure 3K,L,M,N,O* are the cross-sectional B-frames corresponding to the perforated red lines in *Figure 3F,G,H,I,J*, respectively. As was the case with vascular features, each of the structural features mentioned previously are corroborated here with additional information. The eschar, a thickened epidermis, and an epidermal tongue are all visible in *Figure 3M*, and *Figure 3O* shows a thickening epidermis and a brighter dermis immediately below (coinciding with the bright swirled patterns noted in *Figure 3I*).

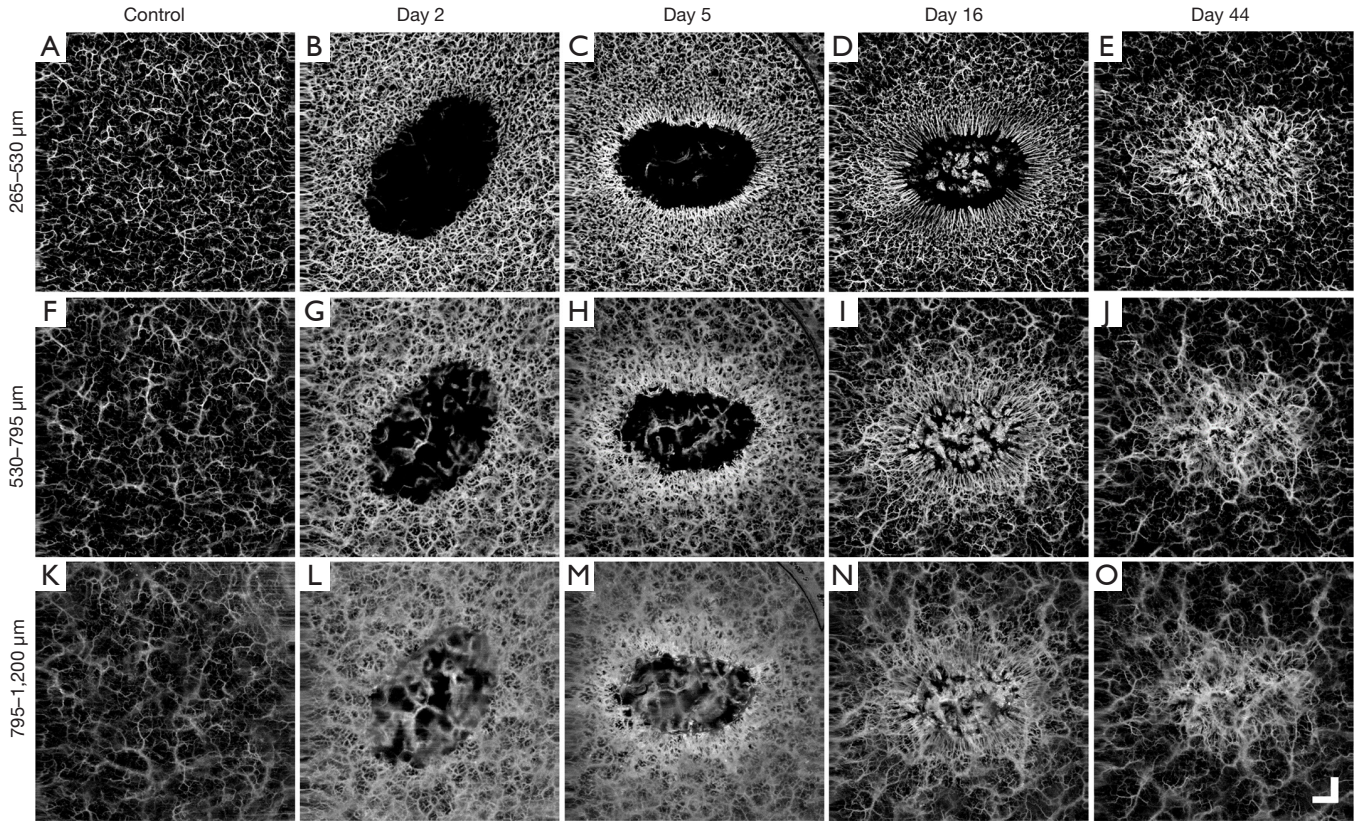

Figure 4 MIP *en face* projected vascular images showing depth-specific vascular features over time. Shown are the three segmented slabs representing the depths of (A,B,C,D,E): 265–530 µm (papillary dermis); (F,G,H,I,J): 530–795 µm (lower papillary/upper reticular dermis); and (K,L,M,N,O): 795–1,200 µm (reticular dermis). From left to right, images are obtained from the scans of normal skin, and wound at day 2, day 5, day 16 and day 44 post-injury, respectively, demonstrating how the vasculatures of different depths respond during healing. Scale bar represents 1 mm. MIP, maximum intensity projection.

Depth-specific vascular features

The depth-specific vascular features over 44-day post-injury are given in *Figure 4*. Shown in *Figure 4A,F,K* are the vascular maps of the papillary dermis, the lower papillary/upper reticular dermis, and the reticular dermis layers, respectively, taken from normal skin. Vascular distribution appears homogenous throughout each of the three anatomic layers; however, both diameter and density appear to be increasing with depth.

Shown in *Figure 4B,C,D,E* are the superficial vessels of the papillary dermis; *Figure 4G,H,I,J* are the vessels of the lower papillary/upper reticular dermis; and *Figure 4L,M,N,O* are the deeper vessels of the reticular dermis, all during healing at time points post-injury as shown. Shown in *Figure 4B,G,L* are uniformly distributed vasodilation surrounding the wound, regardless of vessel depth, and vasodilation within the wound appeared to be dominated by the deeper vessels of the reticular dermis. Angiogenic sprouts are seen only in the uppermost slabs, i.e., the papillary dermis and lower papillary/upper reticular dermis layers (*Figure 4C,H*), and interestingly, these immature angiogenic vessels also appeared brighter than their surrounding counterparts. Shown in *Figure 4D,I,N* is an upsurge in angiogenic sprouting from the reticular dermis. Shown in *Figure 4E,J,O* is vasodilation throughout each of the three vascular layers being located solely within the remodeling wound area.

Depth-specific structural features

The depth-specific structural features over 44-day post-injury are given in *Figure 5*. Shown in *Figure 5A,F,K* are the structures of the papillary dermis, the lower papillary/upper reticular dermis, and the reticular dermis layers,

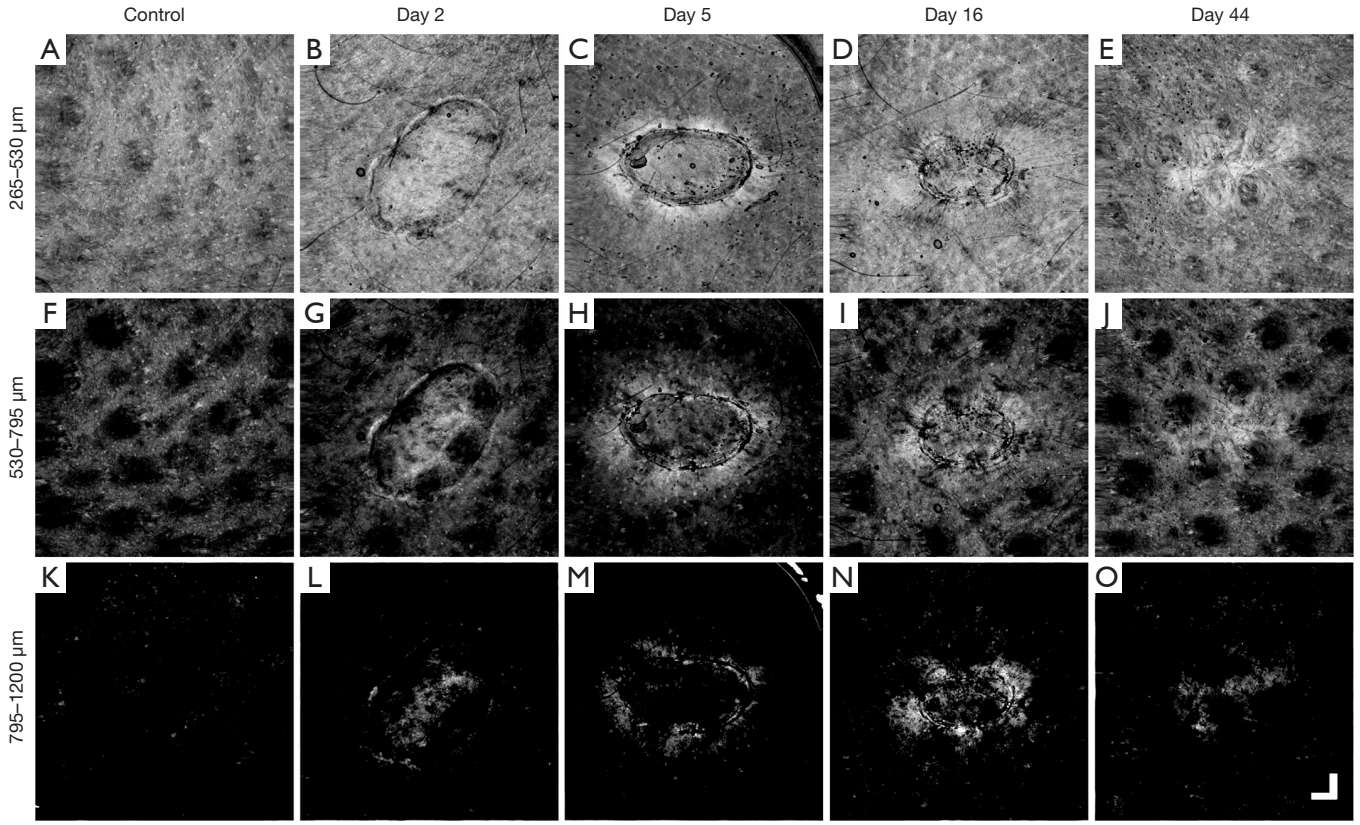

Figure 5 MIP *en face* projected structural images showing depth-specific structural features over time. Shown are the three segmented slabs representing the depths of (A,B,C,D,E): 265–530 µm (papillary dermis); (F,G,H,I,J) 530–795 µm (lower papillary/upper reticular dermis), and (K,L,M,N,O) 795–1,200 µm (reticular dermis). From left to right, images are obtained from the scans of normal skin, and wound at day 2, day 5, day 16 and day 44 post-injury, respectively, demonstrating how the structures of different depths respond during healing. Scale bar represents 1 mm. MIP, maximum intensity projection.

respectively, taken from normal skin. Whilst features differed between each layer, they were all intact and homogenous in distribution.

Shown in *Figure 5B,C,D,E* are the structural features of the papillary dermis; *Figure 5G,H,I,J* are the structural features of the lower papillary/upper reticular dermis; and *Figure 5L,M,N,O* are the structural features of the reticular dermis, all during healing. Whilst wound contraction can be clearly seen in the uppermost slabs (*Figure 5B,C,D,E*), the processes of healing are perhaps most evident in the lower papillary/upper reticular dermis (*Figure 5G,H,I,J*). At the earliest time point, *Figure 5G*, tissue structure within the wound appeared to still have features similar to that of undamaged skin (comparing *Figure 5G,F*). However, as shown in *Figure 5H*, structure within the wound has been completely altered. The wound now appeared almost featureless except for bright tissue immediately adjacent. Shown in *Figure 5I*, tissue structure appeared to be normalizing. Shown in *Figure 5E,J,O* are tissue structures across all depths at days 44 post injury, with very similar features to that of normal skin. A swirled pattern thought to be symptomatic of collagen turnover is the only indication that a wound was ever present.

Quantitative measures

Figure 6 provides the quantification results of various vascular parameters. Each of the three vascular slabs throughout each of the six scanning sessions at the days 2, 5, 9, 16, 23, and 44 post-injury, respectively, are represented alongside the control scan. *Figure 6A* shows vessel diameter measurements taken from the whole affected region, i.e., the wound and surrounding skin. In terms of vessel diameter, each of the three vascular layers differed from

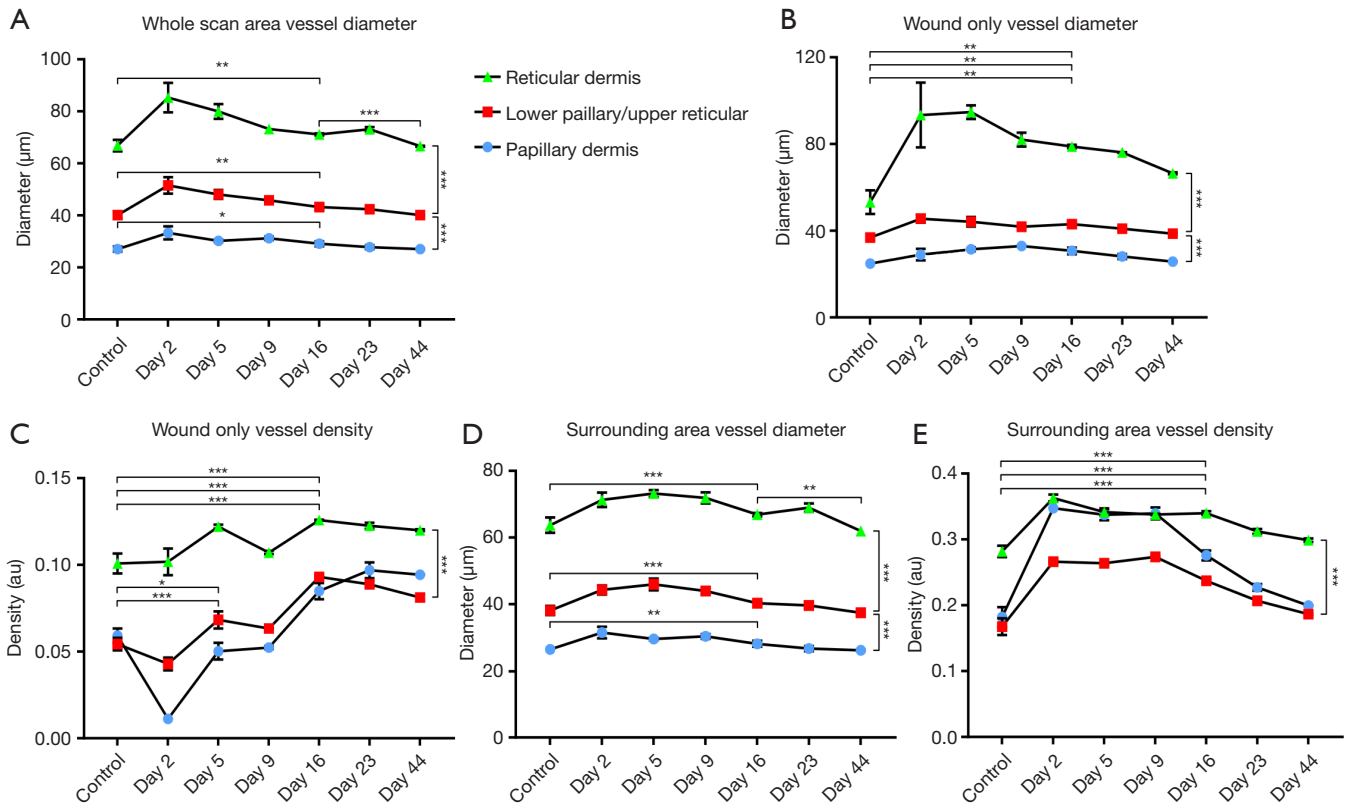

Figure 6 Quantification of vessel parameters from three separate layers spanning the whole healing process. The three separate layers represent vessels from three depths: 265–530 μm (papillary dermis), 530–795 μm (lower papillary/upper reticular dermis), and 795–1,200 μm (reticular dermis). (A) Whole scan area vessel diameter; (B) wound only vessel diameter; (C) wound only vessel density; (D) surrounding area vessel diameter; (E) surrounding area vessel density. Levels of significance are depicted as: *, P≤0.05; **, P≤0.01; ***, P≤0.001; and ****, P≤0.0001.

one another, ranging from approximately 27 μm (±1 μm) in the papillary dermis to approximately 67 μm (±2 μm) in the reticular dermis (one-way ANOVA, P<0.0001). Increased vessel diameter resulting from wounding was most significant in the deeper of the vascular layers and lessened in significance as vasculature became more superficial (lower papillary/upper reticular dermis, one-way ANOVA, P=0.0011; reticular dermis, one-way ANOVA, P=0.0019; papillary dermis, one-way ANOVA, P=0.014). Each of the three layers normalized by day 16. These findings corroborate with the *en face* projected images noted previously (*Figure 3*). The reticular dermis was the only vascular layer to significantly alter after day 16 (one-way ANOVA, P=0.0004); again, corroborating previously noted observations.

Shown in *Figure 6B* are vessel diameter measurements taken solely from within the wound. Again, each of the vascular layers differed from one another, ranging from approximately 25 μm (±1 μm) in the papillary dermis to approximately 53 μm (±5 μm) in the reticular dermis (one-way ANOVA, P<0.0001). Neither vascular layer appeared to have more significant vessel diameter increases compared to the others (papillary dermis, one-way ANOVA, P=0.0065; lower papillary/upper reticular dermis, one-way ANOVA, P=0.0064; reticular dermis, one-way ANOVA, P=0.0043).

Shown in *Figure 6C* are vessel density measurements taken solely from within the wound. In terms of vessel densities, neither of the uppermost vascular layers, i.e., the papillary dermis and lower papillary/upper reticular dermis, differed from one another, but the deeper of the three vascular layers, i.e., the reticular dermis, did (unpaired *t*-test, P=0.0001). In terms of degree of density change in response to healing, all three layers differed from one another. Early on, loss of vessel density was most significant in the most

superficial vascular layer, and lessened thereafter [papillary dermis, one-way ANOVA, P=0.0003; lower papillary/upper reticular dermis, one-way ANOVA, P=0.014; reticular dermis, one-way ANOVA, P=0.06 (ns)]. A similar trend was measured over the duration of the study. Overall alterations in vessel densities were most prominent in the uppermost vascular layers, and lessened thereafter (papillary dermis, one-way ANOVA, P<0.0001; lower papillary/upper reticular dermis, one-way ANOVA, P<0.0001; reticular dermis, one-way ANOVA, P=0.0006). Taken together, these data corroborate visual findings, confirming that the majority of cutaneous damage was located in the uppermost vascular layers.

Shown in *Figure 6D* are vessel diameter measurements taken solely from the surrounding skin of the wound. Each vascular layer differed from one another and increased vessel diameter correlated with increased vessel depth (two unpaired *t*-tests, P<0.0001). With regards to vessel diameter changes in response to healing, vessel diameter increased in all three layers with the degree of significance correlating with vessel depth. That is, the deeper the vessels, the more significant the increase in vessel diameter (papillary dermis, one-way ANOVA, P=0.0049; lower papillary/upper reticular dermis, one-way ANOVA, P=0.0005; reticular dermis, one-way ANOVA, P=0.0006). Vasodilation across all three layers was observed previously (*Figure 4*), but depth-specific degrees of significance were not elucidated from visual inspection. Each layer normalized by day 16, with the reticular dermis being the only vascular layer to increase in diameter again thereafter (one-way ANOVA, P=0.0019). This trend was not noted previously from visual inspection.

Shown in *Figure 6E* are vessel density measurements taken solely from the skin surrounding the wound. Similar to vessel densities measured within the wound, neither of the two uppermost vascular layers, i.e., the papillary dermis and the lower papillary/upper reticular dermis, differed from one another. The deepest of the three layers, however, i.e., the reticular dermis, was more dense (unpaired *t*-test, P=0.0003). Whilst vascular densities increased across all three layers as a response to healing, none of the layers differed from another in terms of degree of significance (papillary dermis, one-way ANOVA, P<0.0001; lower papillary/upper reticular dermis, one-way ANOVA, P<0.0001; reticular dermis, one-way ANOVA, P<0.0001). All three layers normalized by day 16.

Interestingly, when taken together, it appears vessel density changes, particularly in the most superficial vessels, was the dominant response within the wound, whilst vessel diameter changes, particularly in the deeper vessels, was the dominant response in surrounding tissue.

Discussion

In this study, using OCT and OCTA/OMAG, we have non-invasively monitored over time the various vascular and structural characteristics associated with the multiple phases of wound healing in human skin. We were successful in identifying with capillary level resolution, numerous key vascular adaptations and correlate them with structural alterations that are essential elements in the overall processes of healthy wound healing. By analyzing the vascular and structural features outlined in this study, we were able to formulate an approximate wound healing timeline, which includes multiple distinct, yet overlapping phases of the cutaneous wound healing process, i.e., hemostasis, inflammation, proliferation, and remodeling. Shown in *Figure* 7 are the four phases of healing as a timeline schematic. Whilst not all elements of the regenerative process depicted in this figure were directly visualized in this study, they were indirectly visualized via the vascular and structural responses to such elements.

The early phases of wound healing, i.e., hemostasis and inflammation, elicit a number of distinct vascular and structural responses. Here, we observed from the first imaging session a complete loss of superficial vessels within the wound and a significant increase in vessel diameter surrounding the wound. This is typical of partial thickness burns because as they extend to the dermis and damage blood vessels, the immediate response of the microcirculation is to cause coagulation at the wound site and hyperemia in the surrounding areas (60). A similar hyperemic response was noted previously with OCT (61). At this point in the healing process, the increased vasculature was not the result of angiogenesis; rather, the recruitment of pre-existing vessels that previously had little or no blood flow, which was below the minimal velocity that can be detected by OCTA (~4 μm/s) (62). This rationale could be used to explain the vascular measurements noted within this study; in particular, why superficial vessels saw an increase in density over diameter, whilst deeper vessels saw an increase in diameter over density. The onset of the proliferation phase was seen here on the 5th day with the migration of horizontal angiogenic sprouts into the wound, thought to be symptomatic of the recruitment of fibroblasts from adjacent tissues, as well as the differentiation of

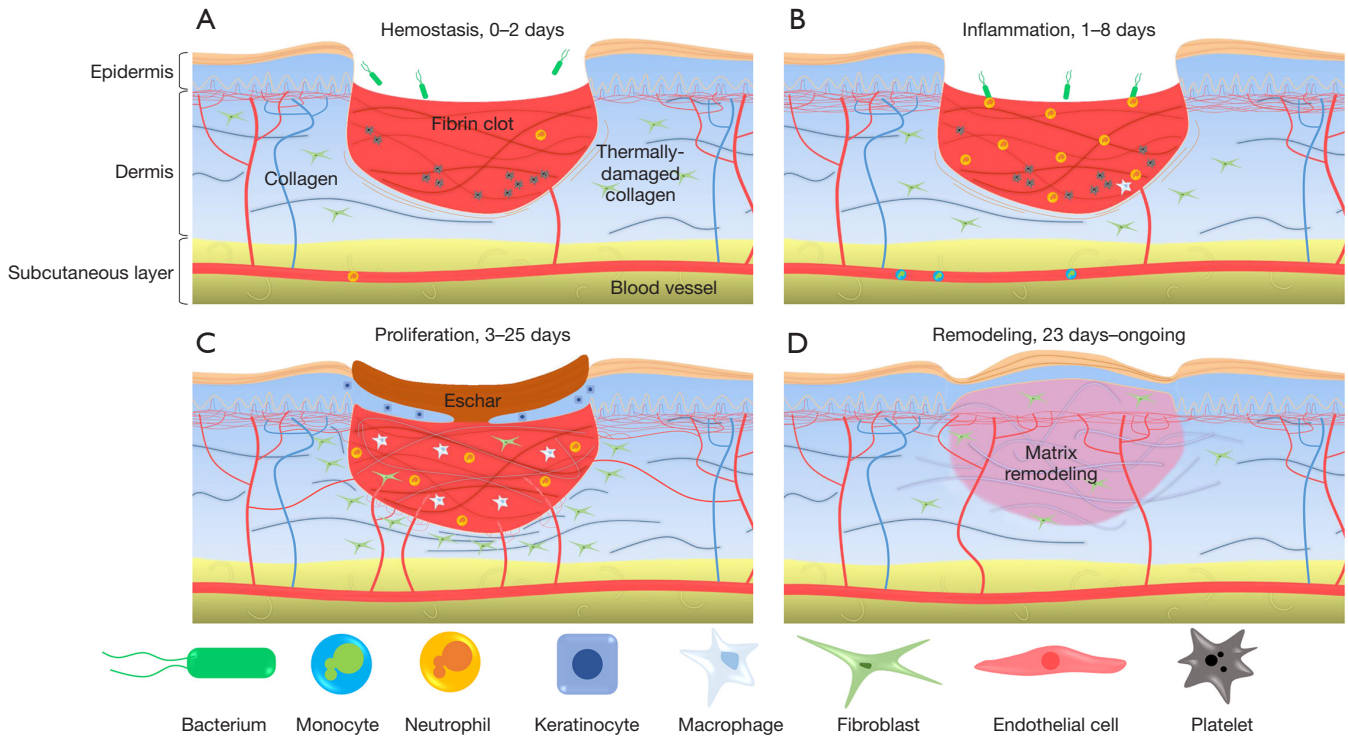

Figure 7 A schematic diagram outlining the multiple phases of wound healing over a timeline. (A) Identifies the first of four phases, hemostasis. Shown is the initial response to the development of the wound, the formation of a fibrin clot; (B) identifies the second phase, inflammation. Shown is the increased capillary blood flow allowing for the augmented migration of cells and other inflammatory products; (C) identifies the third phase, proliferation. Shown is the formation of an eschar, the proliferation of fibroblasts, the formation of an epidermal tongue, i.e., re-epithelialization, and the sprouting of new blood vessels, i.e., angiogenesis; (D) identifies the final phase, remodeling. Shown is thickening of the new epithelium and remodeling of collagen type III to type I.

fibrocytes to fibroblasts (63,64). The early onset of revascularization, i.e., superficial angiogenic sprouts, typically coincides with the onset of re-epithelialization, which can be observed with the tightening of the wound from its edge (65). Here, this tightening also coincided with the appearance of bright structural features. The bright tissue surrounding the contracting wound is thought to be a feature of enhanced collagen deposition (66), which at this stage serves two purposes: to provide structural strength and facilitate the migration of various cell types responsible for wound healing (67,68). This ultimately results in high levels of collagen with relatively low tensile strength, however (69); hence, later remodeling. Interestingly, in this study, increased brightness was not restricted to tissue structure. The angiogenic vessels visualized here also appeared brighter than their surrounding counterparts (*Figure 4*). Studies have shown that the OMAG signal is proportional to the flux of red blood cells passing through the vessels (70,71). Thus, the brighter appearance of the vasculature around the wound may signify an increased volume of red blood cells. This augmented flow subsequently resulted in the increased scattering of light from the red blood cells, which appeared brighter under OCTA. This may have been due, in part, to the leaky nature of angiogenic vessels (72) or to a decreased resistance to flow caused by the formation of new vessels (73) causing a shift in the balance of red blood cell flow. The remodeling phase imaged here coincided with the completion of revascularization and the normalization of vascular parameters surrounding the wound area. Similar observations were noted previously (61). Additionally, the swirled dermal patterns observed here have been linked previously to collagen type III being converted to type I (61,69). This is corroborated by the bright dermis imaged immediately below the now healed wound indicating enhanced collagenous activity (65).

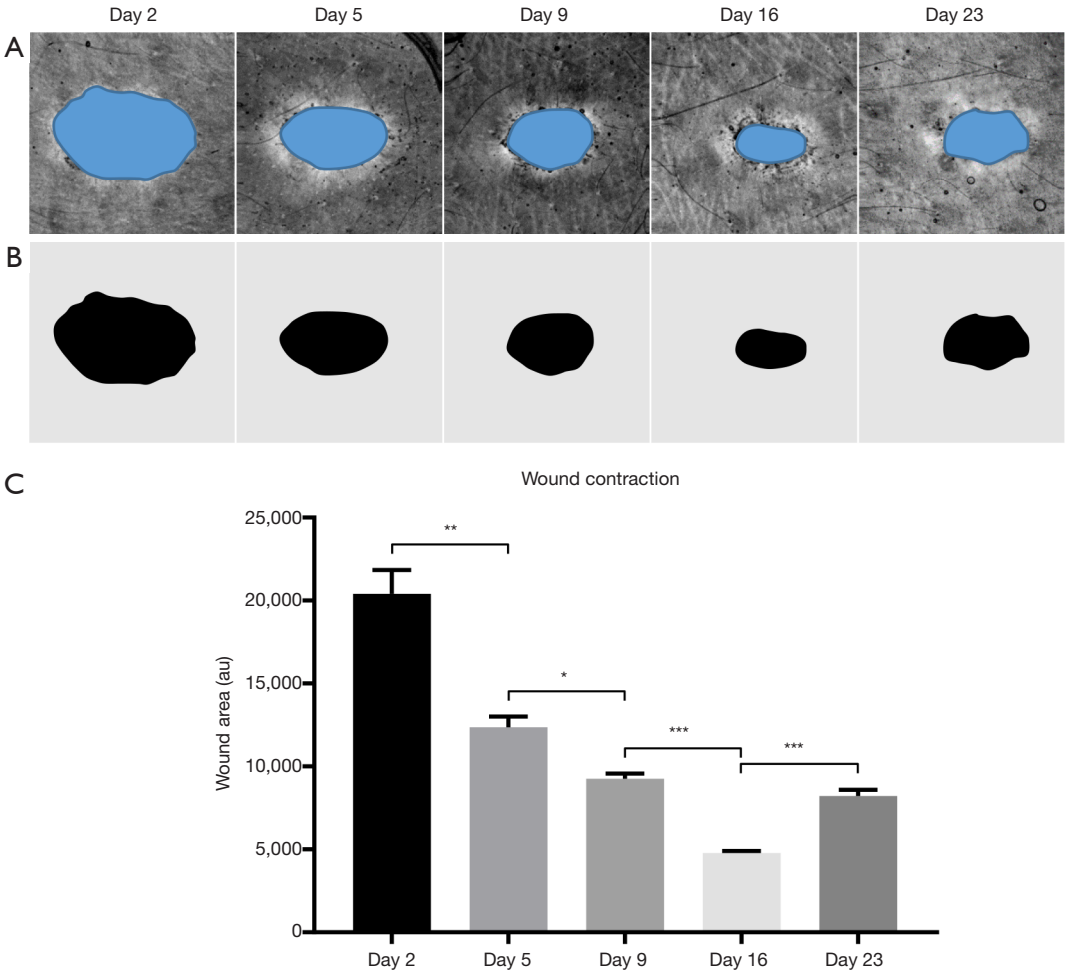

Figure 8 Mask preparation for and quantification of wound contraction. (A) MIP *en face* projected structural images of the wound over the first five of six scanning sessions at the days of 2, 5, 9, 16, and 23 post-injury, respectively. The final scanning session is not included because the wound had healed. The blue area in each image highlights the wound area being masked for quantification; (B) the positive wound masks correlating to each of the images depicted in (A), respectively; (C) wound contraction rate. Levels of significance are depicted as: *, P≤0.05; **, P≤0.01; and ***, P≤0.001. MIP, maximum intensity projection.

One parameter often used in assessing wound healing is wound contraction. Whilst wound contraction rate was measured here (*Figure 8*), it was intended for demonstrative purposes and was not included as a primary measure of healing. This is largely because of what contraction rate means to wound healing in tight-skinned animals, such as humans. In loose-skinned animals, such as mice, measuring wound contraction could be used as a gauge for the health of the healing process because contraction is the primary route of healing in such cases. In humans, however, wound contraction may not be the primary source of wound healing; rather, re-epithelialization is. Wound contraction is typically associated with failed re-epithelialization and unhealthy wound healing in humans, resulting in hypertrophic scarring (74). Additionally, failed re-epithelialization is often associated with chronic wounds (74), which are themselves often associated with pathologies comprising flawed blood flow and/or angiogenic capacities (75). Here, it is suspected that wound contraction was observed alongside the aforementioned vascular response because the wound was of a relatively small size. Should the wound have been larger, the authors believe a measurable vascular response would still be distinguishable, but without observable contraction. With

that, features of revascularization are considered here a more accurate measure of wound healing health given the significant role played by such during re-epithelialization, and the monitoring of specific traits associated with revascularization, such as those demonstrated in this study, could be used to distinguish tissue regeneration, i.e., healthy healing, from tissue repair; i.e., scar formation.

It should be acknowledged, however, that this study is not without limitations. Firstly, the study comprised a single subject, secondly, OCT/OCTA was the sole method of analysis used throughout, and thirdly, the wound analyzed was relatively small in size. Whilst such limitations are inhibiting, they are not detrimental. This study was intended to showcase recent advances in OCT technology and associated analytical techniques via the monitoring of cutaneous wound healing; it was not the authors' intention to hypothesize upon novel medical discoveries, or to prove OCT/OCTA as an all-encompassing diagnostic tool without its own shortcomings. The aforementioned limitations should not take from the validity of the data presented. That being said, however, should OCT/OCTA be used in further studies, a number of adaptations to the study design should be considered. For example, a larger cohort of subjects with a wider array of dermatological injuries would permit the assessment and advancement of OCT technology under different conditions within a variety of scenarios; thus, expanding the applicability of OCT/OCTA. Whilst the vascular and structural features outlined in this study are thought to represent the healing processes via cutaneous regeneration, it is acknowledged that cutaneous repair may offer additional features not represented here. Future studies should include wounds of various depths and severities to possibly establish a threshold whereby regeneration becomes repair, or vice versa. Additional analytical techniques should also be implemented to substantiate the findings of OCT/OCTA. This would allow for further refinement of analytical algorithms and for a more in-depth study in to the various processes involved in wound healing.

In conclusion, OCT/OCTA has provided us with the opportunity to non-invasively image specific vascular adaptations that occur during the numerous stages of human cutaneous wound healing. Additionally, such vascular features have been correlated with structural traits, further adding to the capabilities of this technology. With continued development and refinement, this tool and the information it affords us could be used to assess and monitor wound healing, giving patients more specific and precise treatment options in the future.

Acknowledgements

Funding: The National Heart, Lung, and Blood Institute (R01 HL093140), the National Eye Institute (R01 EY024158), Washington Research Foundation, WRF David and Nancy Auth Innovation Award, and an unrestricted fund from Research to Prevent Blindness. The funding organization had no role in the design or conduct of this research.

Footnote

Conflicts of Interest: Dr. Wang discloses intellectual property owned by the Oregon Health and Science University and the University of Washington related to OCT angiography, and licensed to commercial entities, related to the technology and analysis methods described in parts of this manuscript. Other authors have no conflicts of interest to declare.

Ethical Statement: This study was conducted under a protocol approved by the University of Washington Institutional Review Board (No. 41841).

References

1. Singer AJ, Clark RA. Cutaneous wound healing. N Engl J Med 1999;341:738-46.
2. Diegelmann RF, Evans MC. Wound healing: an overview of acute, fibrotic and delayed healing. Front Biosci 2004;9:283-9.
3. Guo S, Dipietro LA. Factors affecting wound healing. J Dent Res 2010;89:219-29.
4. Pascarella L, Schmid Schönbein GW, Bergan JJ. Microcirculation and Venous Ulcers: A Review. Ann Vasc Surg 2005;19:921-7.
5. Yousefi S, Qin J, Dziennis S, Wang RK. Assessment of microcirculation dynamics during cutaneous wound healing phases in vivo using optical microangiography. J Biomed Opt 2014;19:76015.
6. Cuzzell JZ. The new RYB color code. Am J Nurs 1988;88:1342-6.
7. Wysocki AB. Wound Measurement. Int J Dermatol 1996;35:82-91.
8. Sullivan SR, Underwood RA, Gibran NS, et al. Validation of a model for the study of multiple wounds in the diabetic

mouse (db/db). Plast Reconstr Surg 2004;113:953-60.
9. Powers PS, Sarkar S, Goldgof DB, Cruse CW, Tsap LV. Scar assessment: current problems and future solutions. J Burn Care Rehabil 1999;20:54-60.
10. Bayat A, Mc Grouther DA, Ferguson MW. Skin scarring. BMJ 2003;326:88-92.
11. Yuan Z, Zakhaleva J, Ren H, Liu J, Chen W, Pan Y. Noninvasive and high-resolution optical monitoring of healing of diabetic dermal excisional wounds implanted with biodegradable in situ gelable hydrogels. Tissue Eng Part C Methods 2010;16:237-47.
12. Nettelblad H, Thuomas KA, Sjöberg F. Magnetic resonance imaging: a new diagnostic aid in the care of high-voltage electrical burns. Burns 1996;22:117-9.
13. Iraniha S, Cinat ME, VanderKam VM, Boyko A, Lee D, Jones J, Achauer BM. Determination of burn depth with noncontact ultrasonography. J Burn Care Rehabil 2000;21:333-8.
14. Still JM, Law EJ, Klavuhn KG, Island TC, Holtz JZ. Diagnosis of burn depth using laser-induced indocyanine green fluorescence: a preliminary clinical trial. Burns 2001;27:364-71.
15. Park BH, Saxer C, Srinivas SM, Nelson JS, de Boer JF. In vivo burn depth determination by high-speed fiber-based polarization sensitive optical coherence tomography. J Biomed Opt 2001;6:474-9.
16. Pierce MC, Sheridan RL, Hyle Park B, Cense B, de Boer JF. Collagen denaturation can be quantified in burned human skin using polarization-sensitive optical coherence tomography. Burns 2004;30:511-7.
17. Jeng JC, Bridgeman A, Shivnan L, Thornton PM, Alam H, Clarke TJ, Jablonski KA, Jordan MH. Laser Doppler imaging determines need for excision and grafting in advance of clinical judgment: a prospective blinded trial. Burns 2003;29:665-70.
18. Hoeksema H, Van de Sijpe K, Tondu T, Hamdi M, Van Landuyt K, Blondeel P, Monstrey S. Accuracy of early burn depth assessment by laser Doppler imaging on different days post burn. Burns 2009;35:36-45.
19. Kim KH, Pierce MC, Maguluri G, Park BH, Yoon SJ, Lydon M, Sheridan R, de Boer JF. In vivo imaging of human burn injuries with polarization-sensitive optical coherence tomography. J Biomed Opt 2012;17:066012.
20. Adhi M, Brewer E, Waheed NK, Duker JS. Analysis of morphological features and vascular layers of choroid in diabetic retinopathy using spectral-domain optical coherence tomography. JAMA Ophthalmol 2013;131:1267-74.
21. Chen CL, Wang RK. Optical coherence tomography based angiography (Invited). Biomed Opt Express 2017;8:1056-82.
22. Spöler F, Först M, Marquardt Y, Hoeller D, Kurz H, Merk H, Abuzahra F. High-resolution optical coherence tomography as a non-destructive monitoring tool for the engineering of skin equivalents. Skin Res Technol 2006;12:261-7.
23. Wang RK, Ma Z, Kirkpatrick SJ. Tissue Doppler optical coherence elastography for real time strain rate and strain mapping of soft tissue. Appl Phys Lett 2006;89:144103.
24. Wang RK, Nuttall AL. Phase-sensitive optical coherence tomography imaging of the tissue motion within the organ of Corti at a subnanometer scale: a preliminary study. J Biomed Opt 2010;15:056005.
25. Reif R, Zhi Z, Dziennis S, Nuttall AL, Wang RK. Changes in cochlear blood flow in mice due to loud sound exposure using Doppler optical microangiography and laser Doppler flowmetry. Quant Imaging Med Surg 2013;3:235-42.
26. Srinivasan VJ, Adler DC, Chen Y, Gorczynska I, Huber R, Duker JS, Schuman JS, Fujimoto JG. Ultrahigh-Speed Optical Coherence Tomography for Three-Dimensional and En Face Imaging of the Retina and Optic Nerve Head. Invest Ophthalmol Vis Sci 2008;49:5103-10.
27. An L, Li P, Shen TT, Wang R. "High speed spectral domain optical coherence tomography for retinal imaging at 500,000 A-lines per second." Biomed Opt Express 2011;2:2770-83.
28. Song S, Xu J, Wang RK. Long-range and wide field of view optical coherence tomography for in vivo 3D imaging of large volume object based on akinetic programmable swept source. Biomed Opt Express 2016;7:4734-48.
29. Xu J, Wei W, Song S, Qi X, Wang RK. Scalable wide-field optical coherence tomography-based angiography for in vivo imaging applications. Biomed Opt Express 2016;7:1905-19.
30. Gambichler T, Moussa G, Sand M, Sand D, Altmeyer P, Hoffmann K. Applications of optical coherence tomography in dermatology. J Dermatol Sci 2005;40:85-94.
31. Sattler EC, Poloczek K, Kästle R, Welzel J. Confocal laser scanning microscopy and optical coherence tomography for the evaluation of the kinetics and quantification of wound healing after fractional laser therapy. J Am Acad Dermatol 2013;69:e165-73.
32. Yeh AT, Kao B, Jung WG, Chen Z, Nelson JS, Tromberg BJ. Imaging wound healing using optical coherence tomography and multiphoton microscopy in an in vitro skin-equivalent tissue model. J Biomed Opt 2004;9:248-53.

33. Greaves NS, Iqbal SA, Hodgkinson T, Morris J, Benatar B, Alonso-Rasgado T, Baguneid M, Bayat A. Skin substitute-assisted repair shows reduced dermal fibrosis in acute human wounds validated simultaneously by histology and optical coherence tomography. Wound Repair Regen 2015;23:483-94.
34. Srinivas SM, de Boer JF, Park H, Keikhanzadeh K, Huang HE, Zhang J, Jung WQ, Chen Z, Nelson JS. Determination of burn depth by polarization-sensitive optical coherence tomography. J Biomed Opt 2004;9:207-12.
35. Monstrey S, Hoeksema H, Verbelen J, Pirayesh A, Blondeel P. Assessment of burn depth and burn wound healing potential. Burns 2008;34:761-9.
36. Jaskille AD, Shupp JW, Jordan MH, Jeng JC. Critical review of burn depth assessment techniques: Part I. Historical review. J Burn Care Res 2009;30:937-47.
37. Wang RK, Jacques SL, Ma Z, et al. Three dimensional optical angiography. Opt Express 2007;15:4083-97.
38. Wang RK. Three-dimensional optical micro-angiography maps directional blood perfusion deep within microcirculation tissue beds in vivo. Phys Med Biol 2007;52:N531-7.
39. Wang RK. Optical Microangiography: A Label Free 3D Imaging Technology to Visualize and Quantify Blood Circulations within Tissue Beds in vivo. IEEE J Sel Top Quantum Electron 2010;16:545-54.
40. Zhang A, Zhang Q, Chen CL, Wang RK. Methods and algorithms for optical coherence tomography-based angiography: a review and comparison. J Biomed Opt 2015;20:100901.
41. Baran U, Wang RK. Review of optical coherence tomography based angiography in neuroscience. Neurophotonics 2016;3:010902.
42. Xu J, Song S, Li Y, Wang RK. Complex-based OCT angiography algorithm recovers microvascular information superior to amplitude or phase-based algorithm in phase-stable systems. Phys Med Biol 2017;63:015023.
43. Wang RK, Hurst S. Mapping of cerebro-vascular blood perfusion in mice with skin and skull intact by Optical Micro-AngioGraphy at 1.3μm wavelength. Opt Express 2007;15:11402-12.
44. Reif R, Wang RK. Label-free imaging blood vessel morphology with capillary resolution using optical microangiography. Quant Imaging Med Surg 2012;2:207-12.
45. Chen CL, Zhang A, Bojikian KD, Wen JC, Zhang Q, Xin C, Mudumbai RC, Johnstone MA, Chen PP, Wang RK. Peripapillary Retinal Nerve Fiber Layer Vascular Microcirculation in Glaucoma Using Optical Coherence Tomography–Based Microangiography. Invest Ophthalmol Vis Sci 2016;57:475-85.
46. Wang RK, An L, Francis P, Wilson DJ. Depth-resolved imaging of capillary networks in retina and choroid using ultrahigh sensitive optical microangiography. Opt Lett 2010;35:1467-9.
47. Zhang Q, Wang JG, Wang RK. Highly Efficient Statistical Optical Microangiography Based on Eigen Decomposition. Quant Imaging Med Surg 2016;6:557-63.
48. Le N, Song S, Zhang Q, Wang RK. Robust principal component analysis in optical micro-angiography. Quant Imaging Med Surg 2017;7:654-67.
49. Zhang Q, Lee CS, Chao J, Chen CL, Zhang T, Sharma U, Zhang A, Liu J, Rezaei K, Pepple KL, Munsen R, Kinyoun J, Johnstone M, Van Gelder RN, Wang RK. Wide-field optical coherence tomography based microangiography for retinal imaging. Sci Rep 2016;6:22017.
50. Kam J, Zhang Q, Lin J, Liu J, Wang RK, Rezaei K. Optical coherence tomography based microangiography findings in hydroxychloroquine toxicity. Quant Imaging Med Surg 2016;6:178-83.
51. Kashani AH, Chen CL, Gahm JK, Zheng F, Richter GM, Rosenfeld PJ, Shi Y, Wang RK. Optical coherence tomography angiography: A comprehensive review of current methods and clinical applications. Prog Retin Eye Res 2017;60:66-100.
52. Song S, Xu J, Men S, Shen TT, Wang RK. Robust numerical phase stabilization for long-range swept-source optical coherence tomography. J Biophotonics 2017;10:1398-410.
53. Men SJ. Repeatability of vessel density measurement in human skin by OCT-based microangiography. Skin Res Technol 2017;23:607-12.
54. Xu X, Wang RK. The role of water desorption on optical clearing of biotissue: studied with near infrared reflectance spectroscopy. Med Phys 2003;30:1246-53.
55. Yin X, Chao JR, Wang RK. User-guided segmentation for volumetric retinal optical coherence tomography images. J Biomed Opt 2014;19:086020.
56. Reif R, Qin J, An L, Zhi Z, Dziennis S, Wang R. Quantifying Optical Microangiography Images Obtained from a Spectral Domain Optical Coherence Tomography System. Int J Biomed Imaging 2012;2012:509783.
57. Chu Z, Lin J, Gao C, Xin C, Zhang Q, Chen CL, Roisman L, Gregori G, Rosenfeld PJ, Wang RK.Quantitative assessment of the retinal microvasculature using optical coherence tomography angiography. J Biomed Opt 2016;21:66008.

58. Braverman IM. The cutaneous microcirculation. J Investig Dermatol Symp Proc 2000;5:3-9.
59. Ulrich M, Themstrup L, de Carvalho N, Manfredi M, Grana C, Ciardo S, Kästle R, Holmes J, Whitehead R, Jemec GB, Pellacani G, Welzel J. Dynamic Optical Coherence Tomography in Dermatology. Dermatology 2016;232:298-311.
60. Jackson DM. The diagnosis of the depth of burning. Br J Surg 1953;40:588-96.
61. Greaves NS, Benatar B, Whiteside S, Alonso-Rasgado T, Baguneid M, Bayat A. Optical coherence tomography: a reliable alternative to invasive histological assesment of acute wound healing in human skin? Br J Dermatol 2014;170:840-50.
62. An L, Qin J, Wang RK. Ultrahigh sensitive optical microangiography for in vivo imaging of microcirculations within human skin tissue beds. Opt Express 2010;18:8220-8.
63. Hartlapp I, Abe R, Saeed RW, Peng T, Voelter W, Bucala R, Metz CN. Fibrocytes induce an angiogenic phenotype in cultured endothelial cells and promote angiogenesis in vivo. FASEB J 2001;15:2215-24.
64. García-de-Alba C, Becerril C, Ruiz V, González Y, Reyes S, García-Alvarez J, Selman M, Pardo A. Expression of matrix metalloproteases by fibrocytes: possible role in migration and homing. Am J Respir Crit Care Med 2010;182:1144-52.
65. Kuck M, Strese H, Alawi SA, Meinke MC, Fluhr JW, Burbach GJ, Krah M, Sterry W, Lademann J. Evaluation of optical coherence tomography as a non-invasive diagnostic tool in cutaneous wound healing. Skin Res Technol 2014;20:1-7.
66. Babalola O, Mamalis A, Lev-Tov H, Jagdeo J. Optical coherence tomography (OCT) of collagen in normal skin and skin fibrosis. Arch Dermatol Res 2014;306:1-9.
67. Lawrence WT. Physiology of the acute wound. Clin Plast Surg 1998;25:321-40.
68. .Monaco JL, Lawrence WT. Acute wound healing an overview. Clin Plast Surg 2003;30:1-12.
69. Baum CL, Arpey CJ. Normal cutaneous wound healing: clinical correlation with cellular and molecular events. Dermatol Surg 2005;31:674-86; discussion 686.
70. Chen CL, Bojikian KD, Gupta D, Wen JC, Zhang Q, Xin C, Kono R, Mudumbai RC, Johnstone MA, Chen PP, Wang RK. Optic nerve head perfusion in normal eyes and eyes with glaucoma using optical coherence tomography-based microangiography. Quant Imaging Med Surg 2016;6:125-33.
71. Choi WJ, Qin W, Chen CL, et al. Characterizing relationship between optical microangiography signals and capillary flow using microfluidic channels. Biomed Opt Express 2016;7:2709-28.
72. Thurston G, Suri C, Smith K, McClain J, Sato TN, Yancopoulos GD, McDonald DM. Leakage-resistant blood vessels in mice transgenically overexpressing angiopoietin-1. Science 1999;286:2511-4.
73. Gillies RJ, Schornack PA, Secomb TW, Raghunand N. Causes and effects of heterogeneous perfusion in tumors. Neoplasia 1999;1:197-207.
74. Chen D, Hao H, Fu X, Han W. Insight into Reepithelialization: How Do Mesenchymal Stem Cells Perform? Stem Cells Int 2016;2016:6120173.
75. Falanga V. Wound healing and its impairment in the diabetic foot. Lancet 2005;366:1736-43.

Cite this article as: Deegan AJ, Wang W, Men S, Li Y, Song S, Xu J, Wang RK. Optical coherence tomography angiography monitors human cutaneous wound healing over time. Quant Imaging Med Surg 2018;8(2):135-150. doi: 10.21037/qims.2018.02.07

